electronics

MDPI

Article

Research on the Effect of Nonlinear Variation in Insulation Resistance on the Voltage Divider Ratio of 2 × 550 kV DC Voltage Proportional Standard Device

Yin Gao [1], Ximing Chen [1], Yuqing Duan [1], Ran Gao [1], Chao Wang [1], Zheng Chen [1], Fei Lin [1], Lei Zhuang [1], Wanjun Zhu [2,3], Min He [2,3] and Liang Qin [2,3,*]

[1] State Grid Anhui Electric Power Company Limited, Hefei 230601, China; gaoy2015@ah.sgcc.com.cn (Y.G.); chenxm0011@ah.sgcc.com.cn (X.C.); duanyq2979@ah.sgcc.com.cn (Y.D.); gaor4536@ah.sgcc.com.cn (R.G.); wangc2259@ah.sgcc.com.cn (C.W.); chenz403x@ah.sgcc.com.cn (Z.C.); linf3325@ah.sgcc.com.cn (F.L.); zhuangl2022@ah.sgcc.com.cn (L.Z.)

[2] Hubei Key Laboratory of Power Equipment & System Security for Integrated Energy, Wuhan 430072, China; 2018302070163@whu.edu.cn (W.Z.); whuhemin@whu.edu.cn (M.H.)

[3] School of Electrical Engineering and Automation, Wuhan University, Wuhan 430072, China

* Correspondence: qinliang@whu.edu.cn; Tel.: +86-189-8617-2977

Abstract: This paper investigates the effect of nonlinear changes in insulation resistance on the accuracy of a 2 × 550 kV DC voltage scaling standard device. As the voltage and electric field strength increase, the insulating material exhibits nonlinear conductivity characteristics, leading to a decrease in the insulation resistance value, which in turn affects the potential distribution and the partial voltage ratio and thus reduces the measurement accuracy of the standard device. In order to study this problem in depth, this paper builds a nonlinear resistance measurement platform for insulating materials, and it fits and analyzes the experimental data using an NCIR neural network (Neural Network for Nonlinear Characteristics of Insulation Resistance). In addition, in this paper, the finite element model of the standard device was established by ANSYS simulation, and the equivalent resistance network model was established by applying MATLAB in order to calculate the variation in the voltage dividing ratio under different voltages. The results of the study showed that the nonlinear variation in insulation resistance significantly affects the voltage division ratio of the standard device, especially at high voltage conditions. Addressing the issue, this paper proposes to optimize the electric field distribution by optimizing the structure of the grading ring and adding a shielding resistor layer to reduce the influence of nonlinear effects. Simulation results show that the addition of a second layer to the shielding resistor can effectively improve the measurement accuracy of the device, and the reduction in voltage division ratio error is significant. Compared with the case of a shielding resistor with only one layer, the voltage divider ratio was reduced from 109,998.203 to 109,998.994, and the relative error was reduced 44%, changing from 1.634×10^{-5} to 9.15×10^{-6}. The above study provides an optimized solution for achieving high-precision DC voltage measurement.

Keywords: DC voltage proportional standard device; BP neural network; insulation resistance

Academic Editor: Pedro J. Villegas

Received: 8 November 2024
Revised: 18 December 2024
Accepted: 31 December 2024
Published: 31 December 2024

Citation: Gao, Y.; Chen, X.; Duan, Y.; Gao, R.; Wang, C.; Chen, Z.; Lin, F.; Zhuang, L.; Zhu, W.; He, M.; et al. Research on the Effect of Nonlinear Variation in Insulation Resistance on the Voltage Divider Ratio of 2 × 550 kV DC Voltage Proportional Standard Device. *Electronics* **2025**, *14*, 138. https://doi.org/10.3390/electronics14010138

1. Introduction

An unbalanced distribution of energy resources and load centers in China determines that the power and energy pattern of 'sending electricity from the west to the east' and 'sending electricity from the north to the south' will remain unchanged in the next

40 years [1,2]. Against this background, the development of high-voltage direct current transmission is particularly important. High-voltage DC transmission not only enables flexible control of power transmission across large areas but also has the advantages of low loss and high reliability, thus guaranteeing the optimal allocation of large-scale resources throughout the country. With the advancement of China's energy strategy, the position of high-voltage DC transmission in guaranteeing national energy security will become more and more important. The accurate measurement of DC high voltage is the basis for ensuring the safe, stable and economic operation of the DC transmission system, which is of great significance for maintaining national energy security [3–5].

China has put into operation the world's highest voltage level, largest transmission capacity and longest transmission distance DC transmission project: the Changji-Guquan ±1100 kV DC transmission project. However, a high-accuracy 1100 kV DC voltage ratio standard device has not yet been established, and the corresponding 1100 kV DC voltage ratio value on-site transmission technology is not yet mature, resulting in the inability to trace the 1100 kV DC voltage ratio value, affecting the safety of system operation.

With the increasing voltage level, the nonlinear problem of insulating materials gradually comes to the fore. The electron emission from its surface and the air ionization effect along the surface are enhanced, resulting in a nonlinear decrease in the surface resistance [6,7]. At the same time, the electronic conductivity and electro-dissociation effects within the insulating material are also enhanced, resulting in a similarly nonlinear decrease in body resistance [8,9]. These factors lead to a nonlinear decrease in overall insulation resistance with increasing voltage, which triggers uneven potential distribution.

The nonlinearity of the insulation resistance of the casing of the 1100 kV standard unit and the 550 kV auxiliary standard unit is a problem that will become more serious when tracing back the 1100 kV DC voltage proportional measurements, resulting in a more uneven distribution of the longitudinal casing potentials. At the same time, potential differences of up to tens of kilovolts in the radial direction are generated due to a significant increase in the difference in the point distribution of resistance within the device [10]. In the case of traceability using the improved DC voltage addition method, due to the series connection of the two 550 kV auxiliary standard units, the tips in the middle of the upper and lower sections require a grading ring to control and balance voltage. If the grading ring is in potential suspension, it will have an adverse effect on the experiment and needs to be connected to the insulation and shielding resistors for potential clamping. However, as shown in Figure 1, due to the nonlinear variation in the insulation resistance, the potential of the midpoint of the shielding resistor fluctuates considerably and generates a potential difference with the measuring resistor, which in turn triggers a large leakage current in the support structure, significantly affecting the accuracy of the measured current. This not only reduces the measurement accuracy of the 550 kV auxiliary standard device but also seriously affects the accuracy of the proportional value coefficient of the 1100 kV DC voltage determined by the DC voltage addition test, thus affecting the accuracy of the entire measurement system.

At present, many scholars have carried out a large number of studies on the behavior of nonlinear characteristics of insulation resistance of specific electrical equipment under different operating environments. For example, Sharifi et al. performed a comprehensive transient finite element analysis for the computational problem of multi-dielectric systems with nonlinear field-dependent materials, and they explored the effect of the longitudinal component of the electric field on the normal component of the electric field as well as on the surface of the coils by simulating the system with nonlinear field-dependent materials [11]. Schmerling et al. applied materials with nonlinear dielectric properties to rotating electric machines and developed a new filler material to control the electrical parameters of the stator end winding insulation system [12]. Alireza et al. investigated the effect of nonlinear levels of conductivity on the distribution of electric and temperature fields at pulsed voltages [13]. Li et al. studied the moisture–heat aging characteristics of epoxy resin curing compounds for insulating encapsulation and investigated the effect of aging temperature on their dielectric properties. In order to study the effect of temperature on the nonlinear resistance characteristics of different antihalation materials [14]; Zhang et al. proposed a measurement method using a preset low-resistance strip as an electrode to test the nonlinear voltametric characteristics of four antihalation materials at different temperatures [15]. The research on resistors in DC UHV proportional standard devices is mostly focused on measuring resistance. For example, reference [16] studied the temperature coefficient of resistors and how to eliminate humidity dependence and control leakage current in the high-voltage arm. Reference [17] studied the nonlinear changes of resistance under DC low voltage with temperature and humidity. In summary, it can be seen that there are few corresponding studies at home and abroad on the nonlinear change in the insulation resistance of the DC UHV proportional standard device and the influence of this nonlinear change on the voltage division ratio of the standard device.

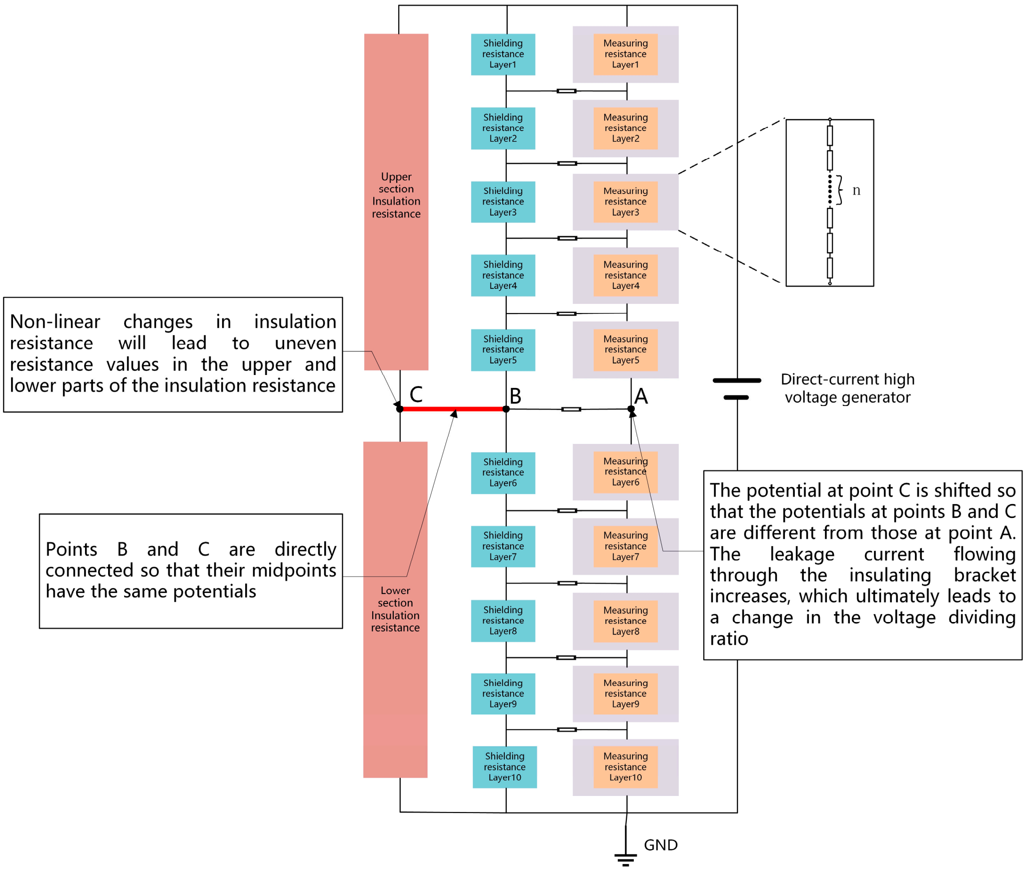

Figure 1. Illustration of the effect of nonlinear changes in insulation resistance on a 2 × 550 kV DC voltage ratio standard device.

To address the above issues, the work in this paper is divided into the following points:

First, a nonlinear resistance measurement platform for the insulation material of the standard device is built to analyze the nonlinear change characteristics and formation mechanism of the insulation resistance with the field strength, study the influence of temperature, humidity and electric field strength on the insulation resistance, design the NCIR neural network to fit and analyze the experimental data, and obtain the relationship between the insulation resistance value and temperature, humidity and electric field strength.

Secondly, the finite element model of the 2 × 550 kV DC voltage ratio standard device is constructed using ANSYS 2022 R1 simulation software, and the electric field distribution around it is calculated and analyzed. The insulation resistance of the standard device is divided according to the electric field strength, and the electric field strength is brought into the neural network obtained above for calculation to obtain the insulation resistance value at this time. The equivalent resistance network model of the 2 × 550 kV DC voltage ratio standard device is established in MATLAB for the subsequent calculation of the voltage divider ratio.

The insulation resistance value, measurement resistance value, shielding resistance value and insulation bracket resistance value are substituted into the equivalent resistance network model to calculate the influence of the nonlinear change in insulation resistance on the accuracy of the voltage divider ratio of the standard device from 50 kV to 1100 kV. Finally, a method of adding a shielding resistance layer is proposed, and its effectiveness is verified by simulation comparison. Experimental results show that adding a shielding resistor layer significantly improves the voltage divider ratio accuracy of the standard device.

2. Analysis of Nonlinear Characteristics of Insulation Resistance

2.1. Theory of Nonlinear Conductance of Insulating Materials at High Field Strengths

The conductivity properties of solid insulating materials under high electric fields are significantly different from the conventional conductivity behavior. While conventional conductance usually follows Ohm's law and exhibits a linear volt–ampere relationship, the conductance of solid insulating materials exhibits non-Ohmic, i.e., nonlinear volt-ampere characteristics under high electric field conditions [18]. At lower electric fields, carriers in polymer media originate from two main mechanisms. One is the formation of intrinsic carriers through thermal excitation, where electrons or holes leap across the energy bands between them, and the other is the production of non-intrinsic carriers through the thermal excitation of impurity energy levels. Due to the typically large forbidden bandwidth of polymers (more than 5 eV), thermal excitation produces very low concentrations of intrinsic and non-intrinsic carriers compared to semiconductors and conductors, and it is not affected by the applied electric field [19].

When a strong electric field is applied to the medium, phenomena such as charge injection near the electrodes or electron emission within the medium may occur, leading to a significant increase in the number of carriers. At this point, the carrier concentration is no longer independent of the applied electric field, but it is significantly elevated with the electric field strength, disrupting the ohmic relationship between the steady-state current density and the electric field strength. Ultimately, the conductivity of the medium varies with the strength of the electric field, exhibiting nonlinear conductivity properties.

For the Schottky effect, the current density is controlled by carriers injected into the medium by thermal excitation of the electrode:

$$j = AT^2 \exp[-\frac{\varphi - \sqrt{e^3 E/4\pi\varepsilon_0\varepsilon_r}}{\mathrm{k}T}] \tag{1}$$

where j is the current density; ε_r is the relative dielectric constant; ε_0 is the vacuum dielectric constant; A is the Richardson–Dushman constant; φ is the work function of the metal; E is the electric field strength; k is the Boltzmann constant; T is the thermodynamic temperature; and e is the electron charge.

For the Poole–Frenkel effect, the conductance change can be described as

$$\frac{j}{E} = \sigma = \sigma_0 \exp[\frac{\sqrt{e^3 E/\pi\varepsilon_0\varepsilon_r}}{\mathrm{k}T}] \tag{2}$$

where j is the current density; E is the electric field strength; σ is the volumetric conductivity; σ_0 is the initial conductivity; e is the electron charge; k is the Boltzmann constant; and T is the thermodynamic temperature.

It can be seen that at high field strengths, if the conductivity mechanism is the Poole–Frenkel effect, the conductivity characteristic curve will be linear in the $ln\ j \sim E^{1/2}$ coordinate system [20].

2.2. Design and Construction of Nonlinear Resistance Measurement Platform for Insulating Materials

In order to realize the measurement of nonlinear resistance of insulating materials, a platform for nonlinear resistance measurement of insulating materials was designed based on relevant principles as shown in Figure 2.

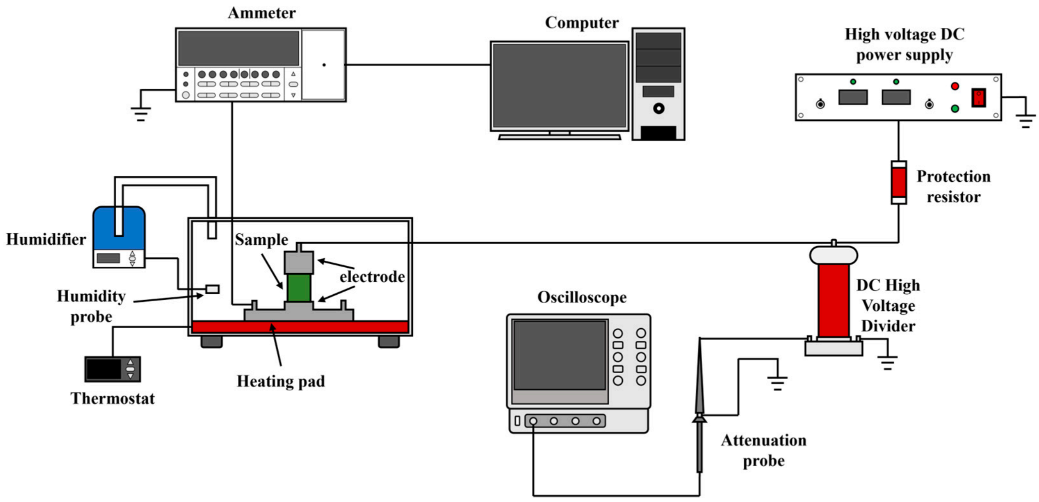

Figure 2. Schematic diagram of nonlinear resistance measurement platform for insulating materials.

The high-voltage DC power supply adopts the TRC2020 series high-voltage power supply, which is equipped with digital voltage and current indication and can be installed in a standard cabinet. It can achieve a linear and smooth rise in high-voltage output from 0 V to 30 kV, meeting the requirements of drawing a curve of the current density of the material under test as the strength of the external electric field changes. The output voltage can be set between 0 V and the highest voltage (the highest voltage output from 1 kV to 30 kV is optional) using the multi-turn potentiometer on the power panel, and the output current can also be set between 0 A and the highest current. The high-voltage power supply has stable performance, and the voltage regulation rate and current regulation rate relative to the input are only ±0.01%. Based on the working electric field strength of the DC UHV standard device, the electric field strength applied to the sample is set to a gradient of 2.5×10^4 V/m, from 2.5×10^4 V/m to 5×10^5 V/m. Considering that the sample may still have some space charge remaining in the previous experiment, it cannot be completely released even if it is short-circuited for a period of time, which will affect the next measurement. Therefore, it is necessary to measure in order from low to high field strength.

The standard resistor used in the experiment is a glass glaze film high-voltage resistor. The resistance of the resistor is 5 MΩ, the power is 200 W, and there is an error of ±5%.

The voltage divider ratio of the DC high-voltage divider used in the experiment is 1000:1, and the uncertainty is 1×10^{-2}.

For the oscilloscope, we used a Dingyang SDS3104X oscilloscope (Shenzhen, China), and the low-voltage arm of the DC high-voltage divider was connected through a

10× attenuation probe, so that its reading was in a ratio of 1:10,000 to the actual voltage applied to the sample. In this way, the voltage applied to the sample was measured, and the output voltage of the high-voltage DC voltage was adjusted according to the reading of the oscilloscope.

The thermostat was connected to the heating pad to adjust the measurement temperature. The heating pad can generate a temperature condition of 30~120 °C. At the same time, the thermostat contains a thermocouple, which can reflect the current temperature in real time. By comparing with the set target temperature value, the operation and stop of the heating pad can be controlled, thereby achieving the purpose of controlling the measurement environment temperature. Based on the operating temperature conditions of the UHV DC standard device, the temperature conditions for measurement are set to 20 °C, 25 °C, 30 °C, 35 °C and 40 °C, respectively.

The humidity environment for measuring the nonlinear resistance of the insulating material is controlled by a humidifier. The humidity probe entering the box reflects the measured humidity conditions in real time, and the real-time humidity is fed back to the humidifier, which is displayed on the humidifier screen. By comparing with the set humidity, the start and stop of the humidifier is controlled, thereby achieving the purpose of controlling the humidity of the measured environment. Based on the operating environment humidity conditions of the DC UHV standard device, the measured ambient humidity is set to 40%, 50%, 60%, 70% and 80%, respectively.

The hollow insulating tube used as the sample uses the common glass fiber winding tube on the market. The product has the characteristics of strong corrosion resistance, light weight and high hardness, good electrical and thermal insulation, good designability and good frost resistance. It is widely used in the field of high-voltage electrical insulation. In order to facilitate the measurement of the current passing through the sample, the specifications of the sample are set to an outer diameter of 32 mm, an inner diameter of 22 mm and a length of 40 mm.

The electrode material used to apply an external electric field to the sample is brass, which has a resistivity of only 2.65 μΩ·cm, excellent thermal and electrical conductivity, and high plasticity. It is widely used in hot and cold pressure processing, and it is used to produce brushes and other products with high conductivity requirements.

The ammeter used to measure the current passing through the sample is a Keithley 6485 picoammeter, which has a minimum theoretical measurement accuracy of 10^{-14} A. The computer is used to automatically collect and save test data. Under different temperature, humidity and field strength conditions, the experimental data record the current curve of the sample during the 180 s pressurization process. Finally, the corresponding current density value is calculated based on the average value of the current measurement results of the last 9 s and the size of the electrode. In addition, under the premise that the current peak does not exceed 50% of the high-precision ammeter range, we tried to select a small range to ensure measurement accuracy.

In order to avoid the influence of surface leakage current on the volumetric current measurement, a three-electrode system was designed as shown in Figure 3. By applying copper foil to the inner and outer surfaces and grounding it, the influence of surface currents is shielded, thus ensuring that the measurement results accurately reflect the conductive current characteristics of the insulating material inside.

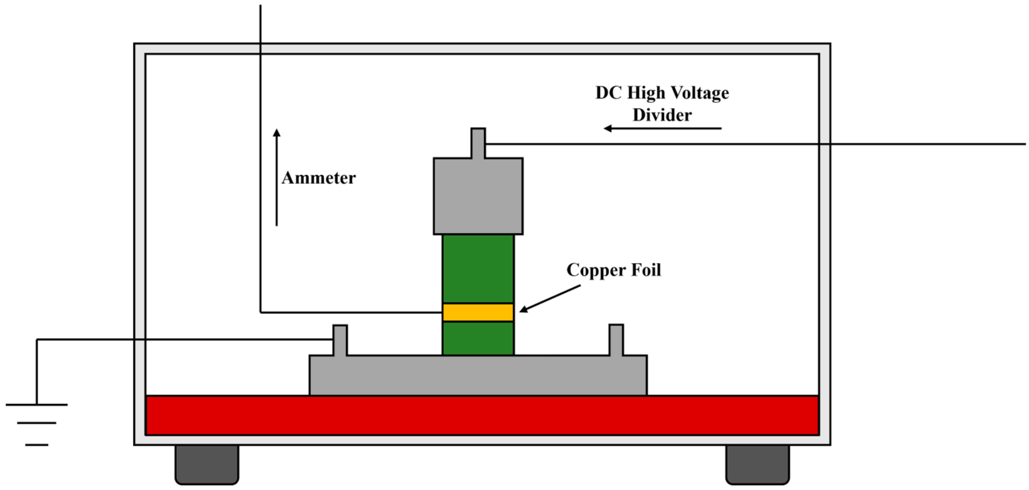

Figure 3. Schematic diagram of an electrode system for measuring volumetric currents in insulating materials.

The electrode system depicted in Figure 4 is designed for measuring the surface current of insulating materials utilized in DC UHV standard devices.

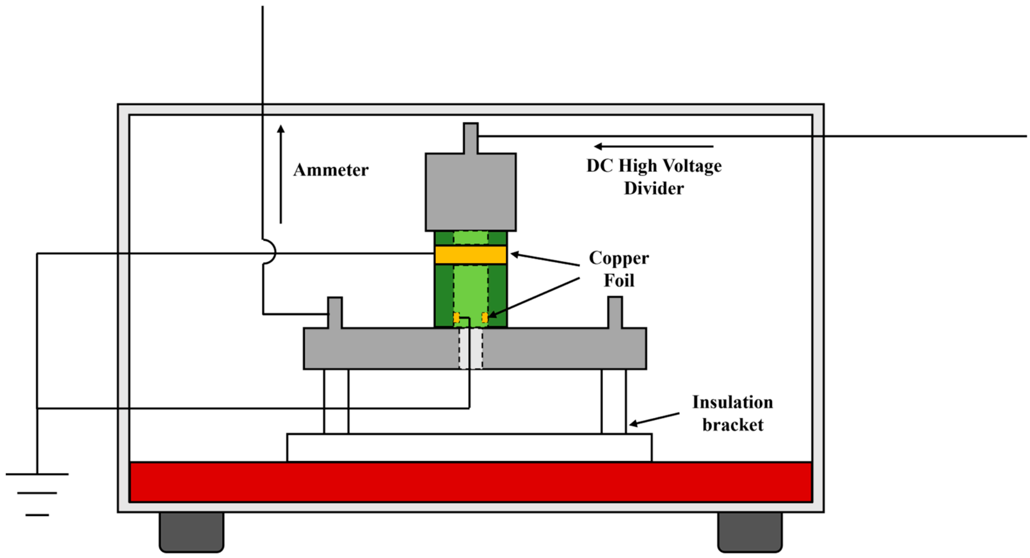

Figure 4. Schematic diagram of electrode system for measuring surface current of insulating materials.

The resistivity of the sample can be determined by examining the relationship between current density and external electric field strength, as depicted in Equation (3). The resistivity ρ can be mathematically represented as

$$\rho = \frac{E}{j} \tag{3}$$

The aforementioned design serves as the foundation for constructing a nonlinear resistance measurement platform for insulating materials used in the DC UHV proportional device as shown in Figure 5.

The data are automatically collected and stored by the computer during the experiment, while recording the current variation under different temperature, humidity, and electric field conditions. In order to ensure that the volume current of the insulating material remains unaffected by surface leakage current during measurement, a specialized electrode system has been devised for precise measurement of both volume current and surface current. Based on the above design, a nonlinear resistance measurement platform for insulating materials used in the DC UHV proportional device is constructed, as shown in Figure 5. During the experiment, the variation ranges of temperature, humidity and electric field intensity are as follows (Table 1):

Table 1. The range of temperature, humidity and electric field strength.

The Structural Parameters	The Range of Values
H (°C)	20–40
W (%)	40–80
E (V/m)	2.5×10^4–5×10^5

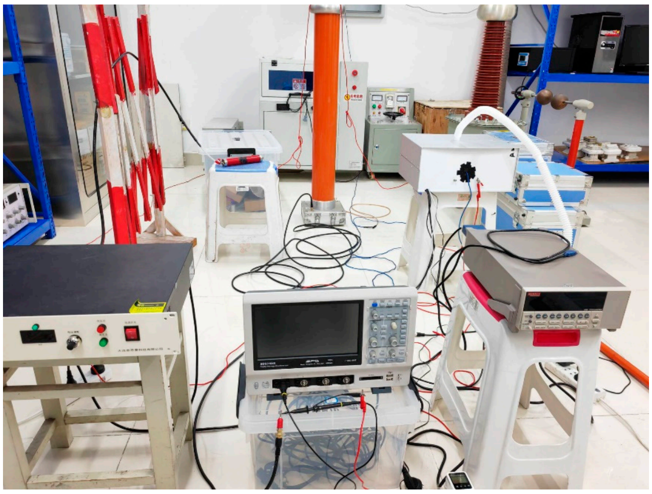

Figure 5. Nonlinear resistance measurement platform for insulating materials used in DC UHV proportional device.

2.3. Experimental Results and Analysis

The experimental results obtained by measurement are shown in the following two groups of figures. When the temperature is constant, the comparison of the resistivity of the insulation resistance with the change in the electric field strength and humidity is as follows (Figure 6).

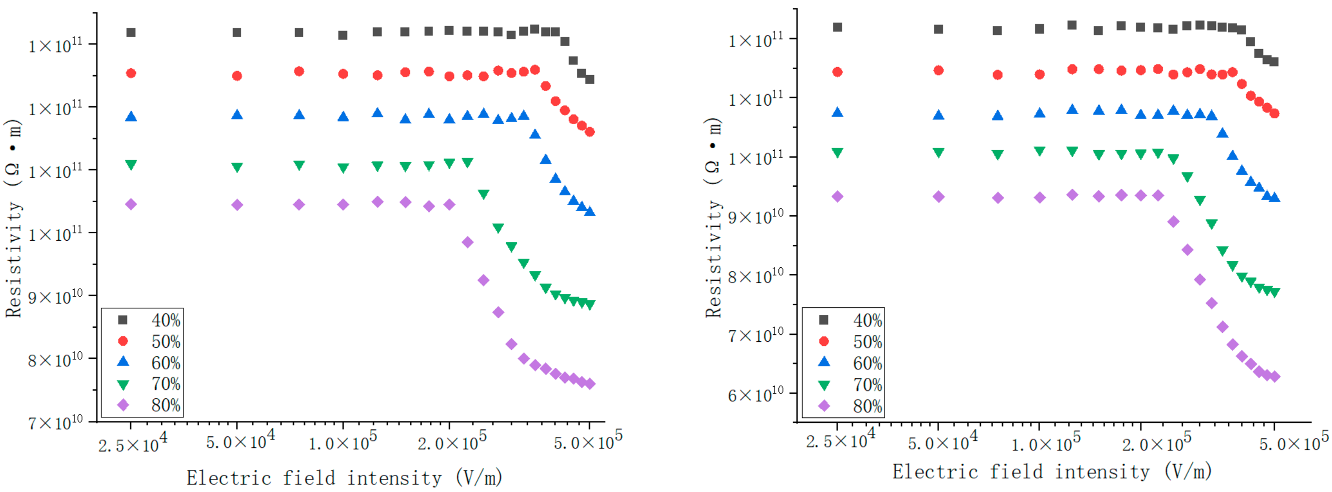

(**a**) (**b**)

Figure 6. *Cont.*

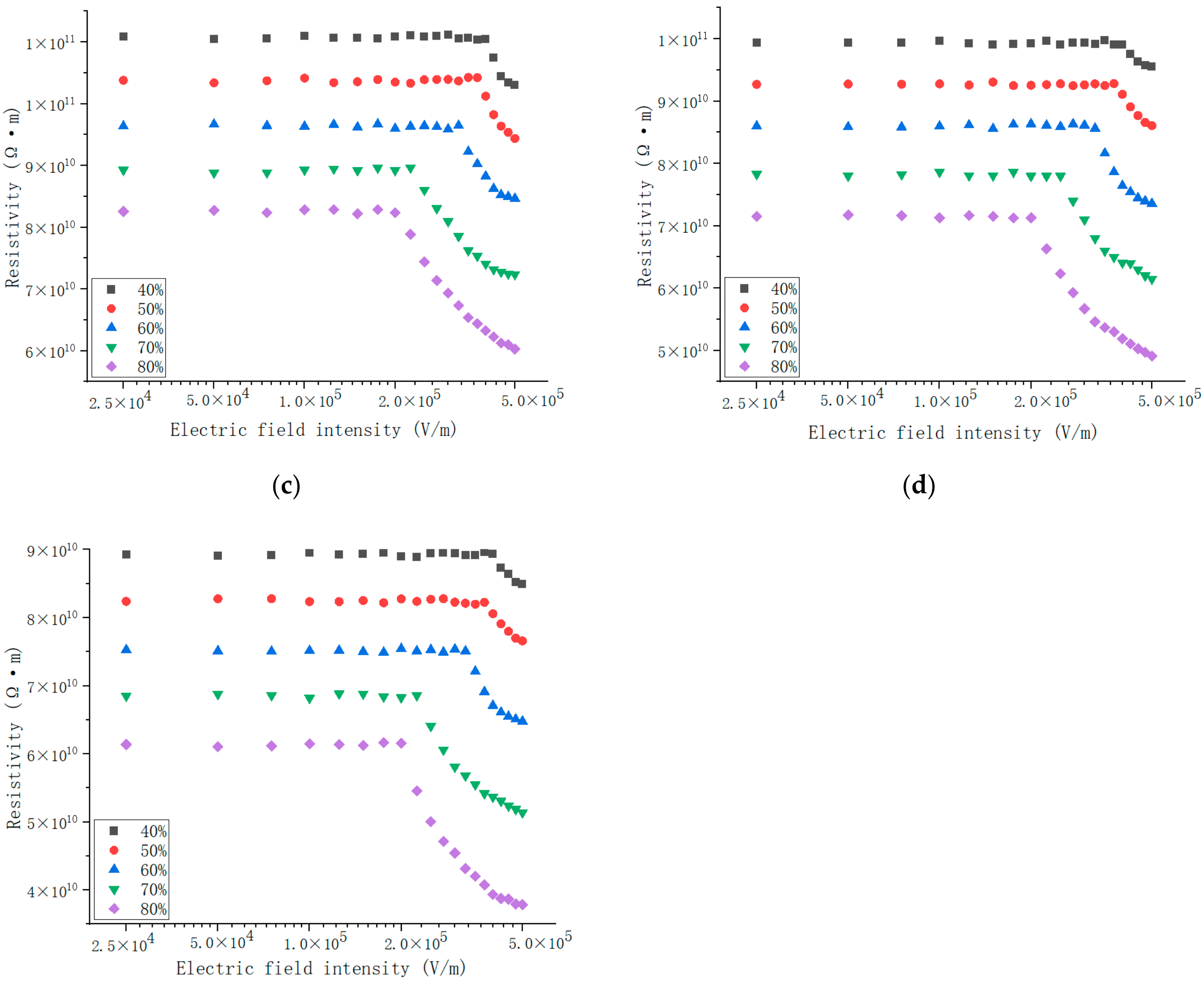

(e)

Figure 6. When the temperature is constant, the resistivity changes with humidity and electric field strength. (**a**) Resistivity change diagram when the temperature is 20 degrees; (**b**) resistivity change diagram when the temperature is 25 degrees; (**c**) resistivity change diagram when the temperature is 30 degrees; (**d**) resistivity change diagram when the temperature is 35 degrees; (**e**) resistivity change diagram when the temperature is 40 degrees.

When the temperature and humidity are constant, as the electric field strength increases, the resistivity hardly changes before a certain electric field strength, and as the electric field strength continues to increase, the resistivity shows a downward trend; when the temperature and electric field strength are constant, the higher the humidity, the smaller the resistivity, and the resistivity changes faster after being subjected to a larger electric field strength.

When the humidity is constant, the comparison chart of the resistivity of insulation resistance changing with the electric field strength and temperature is as follows (Figure 7).

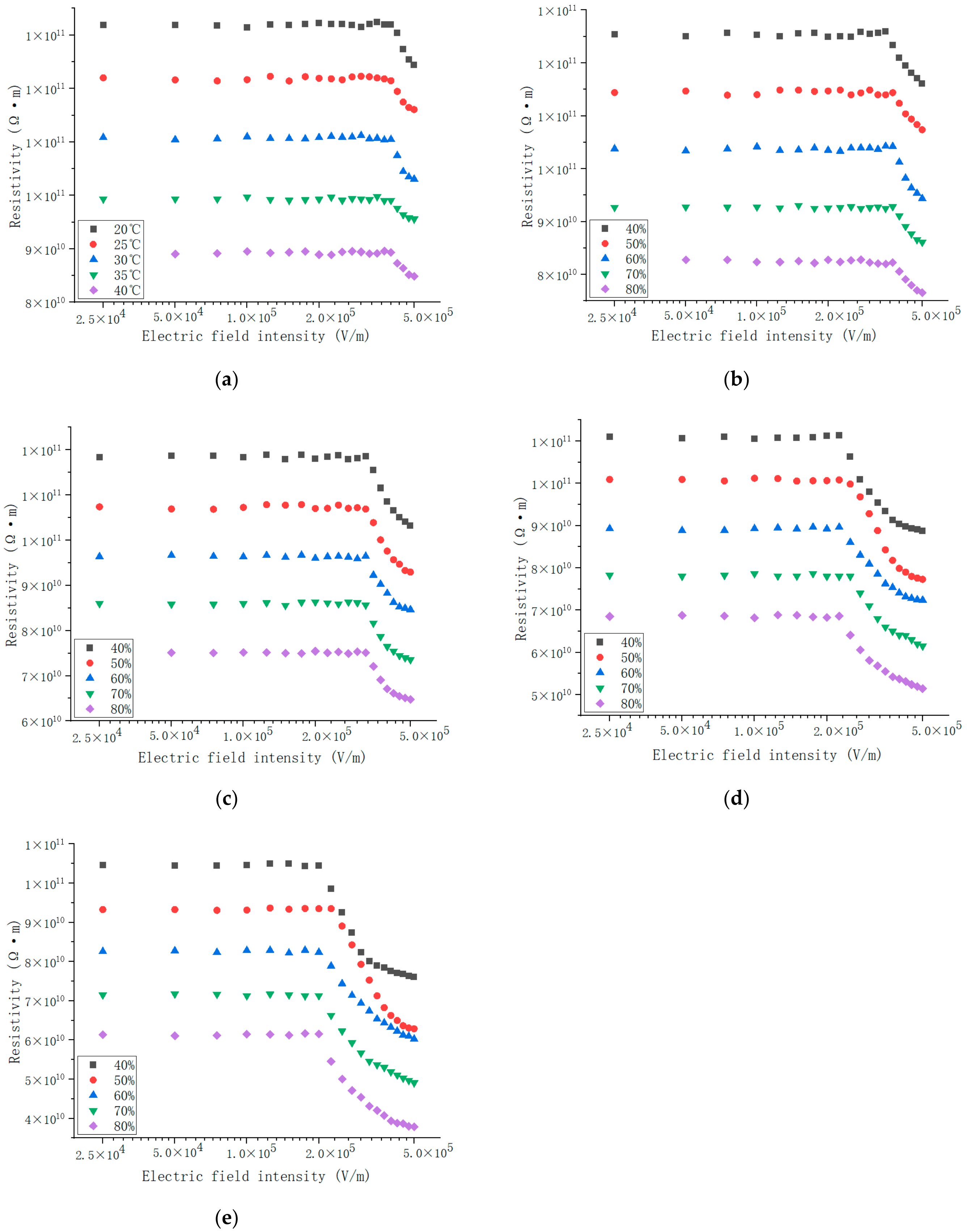

Figure 7. When the humidity is constant, the resistivity changes with temperature and electric field strength. (**a**) Resistivity change diagram when the humidity is 40%; (**b**) resistivity change diagram when the humidity is 50%; (**c**) resistivity change diagram when the humidity is 60%; (**d**) resistivity change diagram when the humidity is 70%; (**e**) resistivity change diagram when the humidity is 80%.

From the above figure, we can see that when the humidity and electric field strength are constant, the higher the temperature, the smaller the insulation resistance. But in general, as the electric field strength increases, the greater the humidity, the greater the change in resistivity, and humidity has a greater impact on the change trend of resistivity.

3. Construction of a Neural Network for Nonlinear Characteristics of Insulation Resistance

3.1. Establishing a Neural Network for the Nonlinear Characteristics of Insulation Resistance

The insulating resistance nonlinear characteristic neural network (NCIR) is established to investigate the impact of electric field intensity, temperature, and humidity on the nonlinear variation in insulating resistance. The NCIR neural network consists of three fully connected layers. The input layer consists of three neurons, which are the normalized parameters of the electric field intensity, temperature and humidity applied to the insulating resistance.

The normalization formula is as follows:

$$X_{norm} = \frac{X - X_{\min}}{X_{\max} - X_{\min}} \tag{4}$$

In the formula, X is raw data, $X_{\min}$ is the minimum value in the dataset, $X_{\max}$ is the maximum value in the dataset, and X_{norm} is the normalized data.

For the deep neural network, the ReLu function is chosen as the activation function for both the input layer and output layer to alleviate the overfitting problem. The ReLu function is as follows:

$$f(x) = \max(0, x) \tag{5}$$

The mapping relationship between electric field strength, temperature, humidity and insulating resistance conductivity can be obtained by the set neural network. The result of the NCIR neural network is shown in Figure 8; the number of nodes in each layer gradually increases and then decreases according to the n-th power of 2. The data are encoded and then decoded, and the selection of the number of model layers is selected by further experimental comparison. The algorithm flow chart of the neural network is shown in Figure 9.

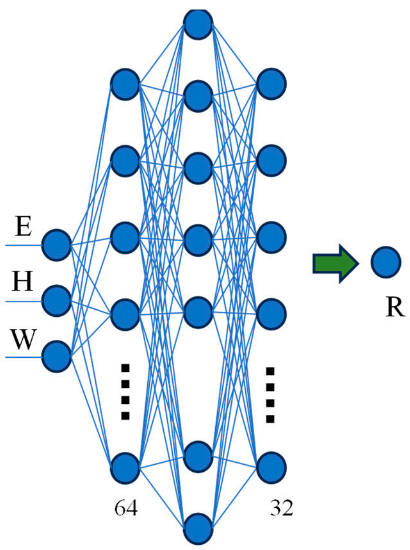

Figure 8. Structure diagram of NCIR neural network. The dots represent neurons, the numbers below represent the number of neurons, and the lines between the dots represent full connections.

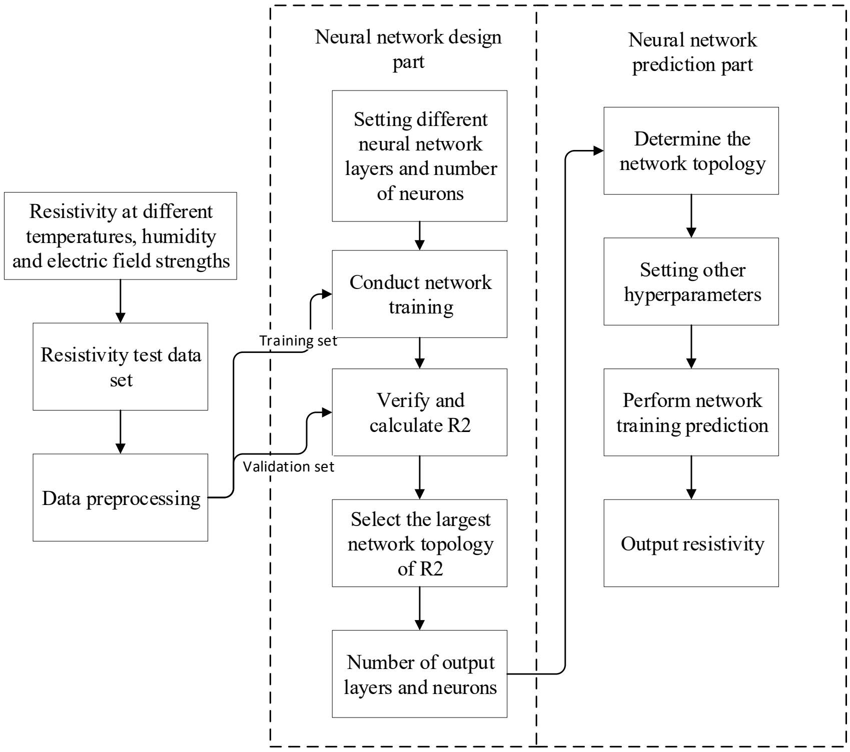

Figure 9. Neural network algorithm flow chart.

3.2. Analysis of Experimental Results

In this paper, the comparative training of neural networks with different layers is carried out in the same experimental environment using the dataset obtained by the experiment in 1.2, including 1100 data samples. The dataset is divided into three parts: the training set, verification set and test set with a split ratio of 8:1:1. In this experiment, the MATLAB version is R2023a, and the neural network training toolbox of MATLAB is used in the neural network training. The training process is accelerated by an NVIDIA GeForce RXT 4060 graphics card. The initial round is set to 100 rounds, the initial learning rate is 0.001, the training function is Levenberg–Marquardt, and the target error is 1×10^{-5}. Default value is used for weights, thresholds and other network parameters.

When measuring the performance of neural networks with different layers, the following three indexes are selected: mean absolute error (MAE), mean square error (MSE), and root mean square error (RMSE). The calculation formulas are as follows:

$$MAE = \frac{1}{n}\sum_{i=1}^{n}|y_i - \hat{y}_i| \tag{6}$$

$$MSE = \frac{1}{n}\sum_{i=1}^{n}(y_i - \hat{y}_i)^2 \tag{7}$$

$$RMSE = \sqrt{MSE} \tag{8}$$

In this paper, the comparative training of multiple models was carried out in the same experimental environment, including support vector machine regression, decision tree regression, random forest regression and neural network regression. The training results are shown in Table 2.

It can be seen from Table 2 that the MAE, MSE, and RMSE of the neural network regression method are the minimum values among the four regression methods. Therefore, the neural network regression can be considered as the optimal method among the four regression methods.

Table 2. Comparative tests using different algorithmic models.

Activation Function	MAE	MSE	RMSE
SVM	0.8971	2.8374	1.6844
Decision tree	0.8867	1.6714	1.2928
Random forest	0.8365	1.0743	1.0365
Neural Networks	0.6728	1.0669	1.0329

The experimental data were normalized and calculated. The experimental results are shown in the following Table 3.

Table 3. Comparative experiments using different numbers of layers in the model.

Number of Fully Connected Layers	MAE	MSE	RMSE
1 layer	0.7939	0.8707	0.9331
2 layers	0.6728	1.0669	1.0329
3 layers	0.5558	0.8459	0.9197
4 layers	0.8587	1.5442	1.2427

It can be seen from the table that when the number of fully connected layers increases from one to three, the MAE, MSE, and RMSE gradually become smaller, and the prediction error of the model gradually becomes smaller. But when the number of fully connected layers continues to increase, the MAE, MSE, and RMSE of the model become larger, and the prediction error becomes larger. This may be due to the over-fitting phenomenon of the model. Therefore, the neural network model of the three fully connected layers is used as the final model of this paper.

The loss curve of neural network training with three fully connected layers is shown in Figure 10.

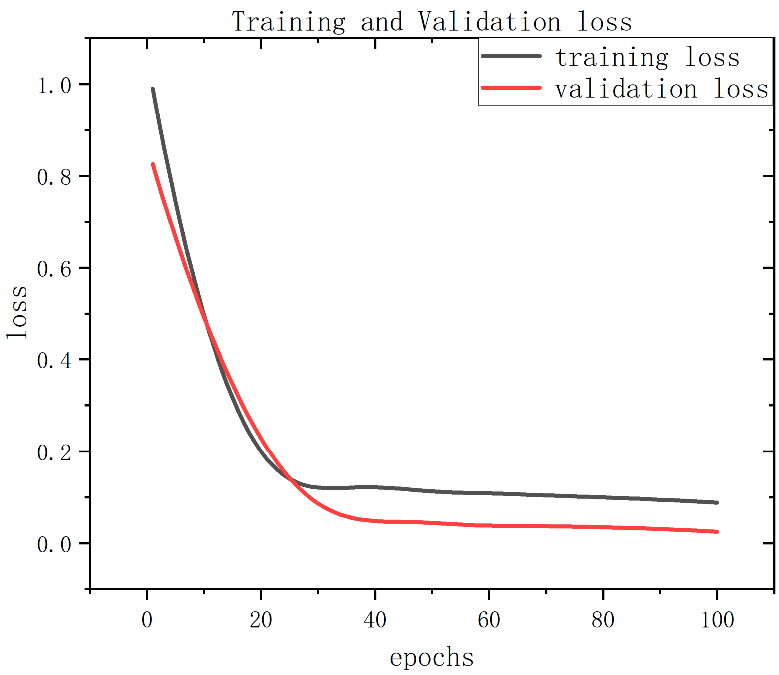

Figure 10. The loss curve.

The diagram illustrates that the loss value of the model is low when the number of fully connected layers is three, and model is in a stable and convergent state between 90 and 100 s.

In order to verify its accuracy under high voltage, this project conducted a measurement experiment of the insulation resistance value of the DC voltage ratio standard device under 550 kV. The voltage was increased from 50 kV to 550 kV, and the insulation resistance value of the single section of the auxiliary standard device and the upper Section 2 after series connection was measured under a certain temperature and humidity. The measurement experiment is as follows (Figure 11 and Table 4).

Figure 11. Experimental platform for insulation resistance measurement at 550 kV.

The measurement results are shown in the following table.

Table 4. Insulation resistance measurement test results at 550 kV.

Temperature (°C)	Relative Humidity (%)	Voltage (kV)	Insulation Resistance (GΩ)
9	56	62.2820	2698
9	56	62.2760	2896
9	56	135.2600	1091
9	56	135.2600	1121
9	56	192.8800	608
9	56	192.8900	620
9	56	259.1000	435
9	56	259.0300	439
9	56	334.0600	326
9	56	333.9400	330
9	56	392.4300	272
9	56	392.3200	275
9	56	450.8000	232
9	56	450.7100	231
9	56	526.0800	185
9	56	561.2310	162

The temperature, humidity, voltage and electric field strength obtained by simulation during measurement are brought into the established NCIR neural network for calculation, and the comparison between the insulation resistance value and the measurement result is shown in the following Figure 12.

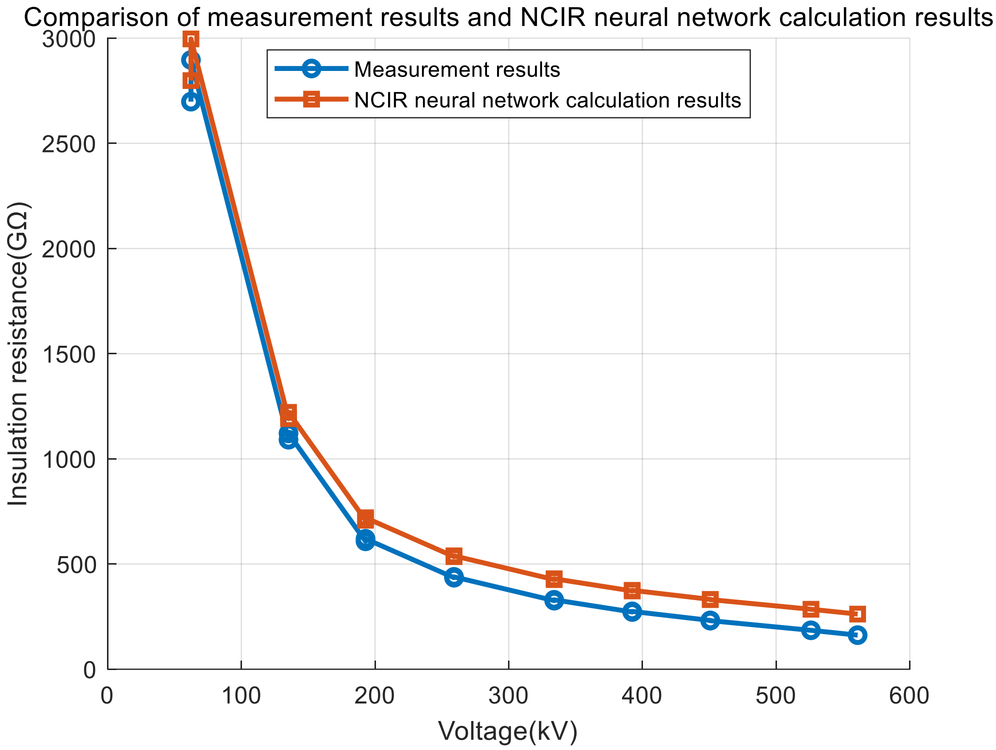

Figure 12. Comparison of insulation resistance measurements with predicted results.

It can be seen that from 50 kV to 550 kV, the calculation results of the NCIR neural network are consistent with the experimental measurement results. Therefore, it can be considered that the calculation results of the NCIR neural network are more accurate.

4. Establishment of Finite Element Model of 2 × 550 kV DC Voltage Proportional Standard Device

In order to obtain the size and distribution of the electric field of the 2 × 550 kV DC voltage proportional device, the model of the 2 × 550 kV DC voltage proportional device can be established by using the simulation software ANSYS, and the infinite domain problem can be transformed into a finite domain problem by the finite element method [21]. The solution of the electric field and potential distribution can be considered as solving the following problems:

In the solution domain:

$$\nabla^2 E = 0 \tag{9}$$

On various media and continuous interface:

$$n(D_1 - D_2) = 0 \tag{10}$$

On the conductor side potential:

$$V_1 = V_0 \tag{11}$$

On finite boundary potential:

$$V_2 = 0 \tag{12}$$

In the formula, E is the electric field strength in the region that needs to be solved, n is the normal direction perpendicular to the interface of the medium, D_1 and D_2 are the electric displacement of the medium on both sides of the interface perpendicular to the interface, V_o is the specific potential value of the conductor side, V_1 is the conductor side potential, and V_2 is the finite boundary potential. In order to ensure the accuracy of the simulation analysis and shorten the calculation time, the solution boundary is divided into three regions. The theoretical analysis indicates that the electric field concentration is highest in the central region, necessitating highest precision. Therefore, emphasis is placed on the core area, which includes the standard device and equalizing ring, where the densest subdivision is carried out. On the contrary, the other two regions are divided relatively sparsely according to the principle of the decreasing distance center [22].

The 2 × 550 kV DC voltage proportional standard device is composed of two 550 kV standard devices in series, including a measuring resistance layer and a shielding resistance layer. Each resistance layer is composed of resistors in series, which are evenly spirally distributed along the insulating inner cylinder from the top to the bottom of the standard device. At the position of each resistance node, the potential of the two resistance layers is very close because the measuring resistance and the shielding resistance are in parallel, and the measuring resistance of each layer is the same as the shielding resistance. Since the resistance of the measuring resistance layer and the shielding resistance layer is evenly distributed from top to bottom, to further simplify the model, they are replaced by two equal cylinders, respectively. Finally, the device is simplified into the 2 × 550 kV standard device with a three-dimensional axisymmetric structure. When constructing the ANSYS finite element model, for the entity of the three-dimensional axisymmetric structure, it can be modeled by taking half of the spindle profile in two dimensions. This approach simplifies the three-dimensional electrostatic field problem into a two-dimensional electrostatic field problem. In this model, the voltage is used as the degree of freedom for the solution of unit nodes, and the DC high voltage at the top of the measuring resistance layer and the outer shielding resistance layer is applied through the high-voltage conductive rod in the calculation of the electrostatic field with the bottom end grounding. The finite element model of the 2 × 550 kV DC voltage proportional standard device is shown in Figure 13.

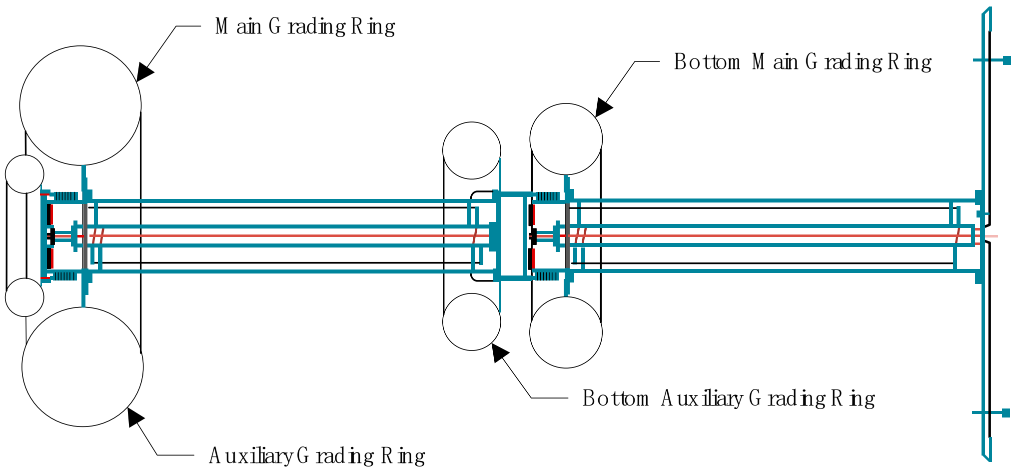

Figure 13. Schematic diagram of 2 × 550 kV DC voltage proportional standard device.

The electric field distribution of the 2 × 550 kV DC voltage proportional standard device is calculated by using simulation calculation. The calculation results are as follows (Figure 14).

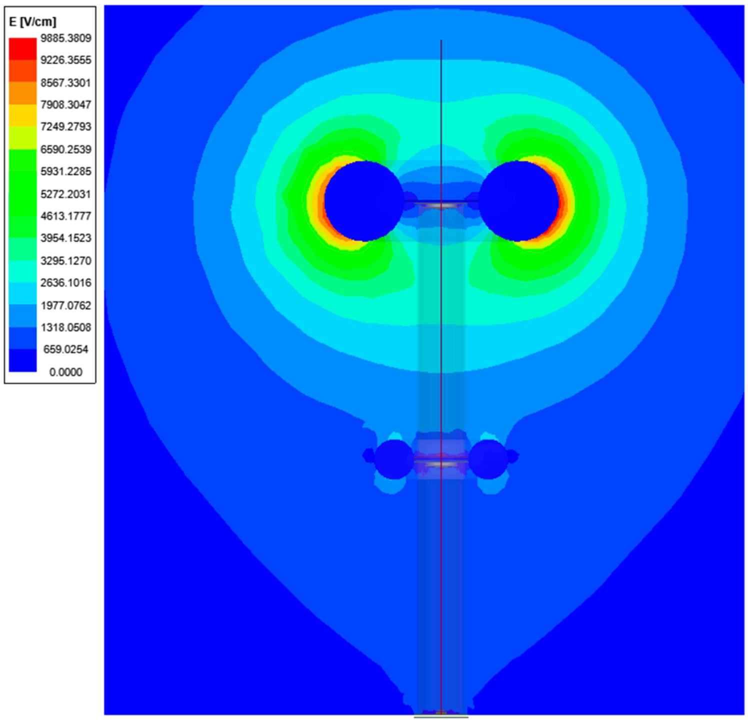

Figure 14. The 2 × 550 kV DC voltage proportional standard device electric field strength and distribution. E in the figure represents the electric field strength in various places.

It can be seen from the above figure that the electric field strength of the upper section of the 2 × 550 kV DC voltage proportional standard device is larger, and the insulation resistance can be divided into four parts according to the distributed field strength. Because the field strength and distribution are inconsistent when different voltages are applied for each time, the upper and lower sections of the insulation resistance are evenly divided into four resistors for convenient calculation, and the electric field strength of each resistor is the average value in this interval. The electric field strength of the 2 × 550 kV DC voltage proportional standard device is calculated respectively under the voltage levels of 50 kV, 100 kV, . . ., 1050 kV and 1100 kV. The field strength of the insulation resistance is divided, the electric field strength of the upper section of insulation resistance is expressed by E_1, E_2, E_3, E_4, and the electric field strength of the lower section of the insulation resistance is expressed by E_1', E_2', E_3', E_4'. The results are shown in Tables 5 and 6 below:

Table 5. The electric field strength of the upper section of insulation resistance.

Number of Fully Connected Layers	E_1 (V/cm)	E_2 (V/cm)	E_3 (V/cm)	E_4 (V/cm)
100	140.910	187.337	263.589	200.512
150	211.192	280.952	394.919	303.955
200	280.631	374.500	525.829	403.843
250	351.112	468.096	656.758	498.920
300	421.437	561.905	787.560	600.699
350	351.112	468.096	656.758	498.920
400	491.984	655.213	918.227	704.865
450	634.232	841.893	1180.203	907.533
500	704.702	935.436	1311.337	1008.370
550	775.172	1028.980	1442.471	1109.207
600	845.642	1122.523	1573.604	1210.044
650	916.112	1216.067	1704.738	1310.881
700	986.583	1309.611	1835.872	1411.718

Table 5. *Cont.*

Number of Fully Connected Layers	E_1 (V/cm)	E_2 (V/cm)	E_3 (V/cm)	E_4 (V/cm)
750	1057.053	1403.154	1967.006	1512.555
800	1127.523	1496.698	2098.140	1613.392
850	1197.993	1590.241	2229.273	1714.229
900	1268.463	1683.785	2360.407	1815.066
950	1338.933	1777.329	2491.541	1915.903
1000	1409.404	1870.872	2622.674	2016.740
1050	1479.874	1964.416	2753.808	2117.577
1100	1550.344	2057.959	2884.942	2218.414

Table 6. The electric field strength of the lower section of insulation resistance.

Number of Fully Connected Layers	E_1' (V/cm)	E_2' (V/cm)	E_3' (V/cm)	E_4' (V/cm)
100	72.529	74.000	85.187	97.098
150	109.314	111.506	128.336	146.140
200	144.941	149.026	171.459	195.117
250	179.241	186.986	214.711	244.650
300	214.956	224.717	257.904	293.829
350	179.241	186.986	214.711	244.650
400	251.047	262.258	301.204	343.417
450	323.720	338.656	388.643	443.598
500	359.689	376.284	431.825	492.887
550	395.658	413.913	475.008	542.176
600	431.627	451.541	518.190	591.465
650	467.596	489.169	561.373	640.753
700	503.565	526.798	604.555	690.042
750	539.534	564.426	647.738	739.331
800	575.503	602.055	690.920	788.619
850	611.472	639.683	734.103	837.908
900	647.441	677.312	777.285	887.197
950	683.410	714.940	820.468	936.486
1000	719.379	752.568	863.650	985.774
1050	755.348	790.197	906.833	1035.063
1100	791.317	827.825	950.015	1084.352

5. The Calculation and Analysis of the Voltage Ratio of the DC Voltage Proportional Standard Device

The above content established a nonlinear resistance measurement platform for insulation materials. The NCIR neural network is designed to fit the experimental results, and the relationship between insulation resistance, field strength, temperature and humidity is obtained. The 2 × 550 kV DC voltage proportional standard device model was established by ANSYS, and the size and distribution of the electric field were obtained. However, the equivalent resistance network model of the 2 × 550 kV DC voltage proportional standard device is needed to calculate the voltage division ratio by combining the above contents.

5.1. 2 × 550 kV DC Voltage Proportional Standard Device Equivalent Resistance Network Model

The instability of the resistor value is the main reason for the change in the voltage division ratio of the DC voltage ratio standard. When establishing the finite element model of the DC voltage proportional standard device, the insulation bracket is simplified because the potential of the two resistance layers of the measuring resistance and the shielding resistance is very close, and the insulation bracket connecting the two resistances has little impact during the electric field simulation. However, when calculating the voltage division ratio, the impact of the insulation bracket cannot be ignored, so there should be an insulation bracket in the resistance equivalent model. Then, the measuring resistance and the shielding resistance should be equivalent to multiple resistors in series, which are connected by insulating brackets. However, there are hundreds of resistances and insulation brackets in the 2 × 550 kV DC voltage proportional standard device. In this paper, they are simplified into resistor modules and connected in series. The insulation outer cylinder is greatly affected by the voltage and field strength, and the field strength acting on the insulation outer cylinder has an uneven distribution. Therefore, the resistance of the insulation outer cylinder is calculated in sections based on the electric field simulation results, and it is equivalent to multi-section resistance in series in the end. The resistance network model of the 2 × 550 kV DC voltage proportional standard device is shown in Figure 15.

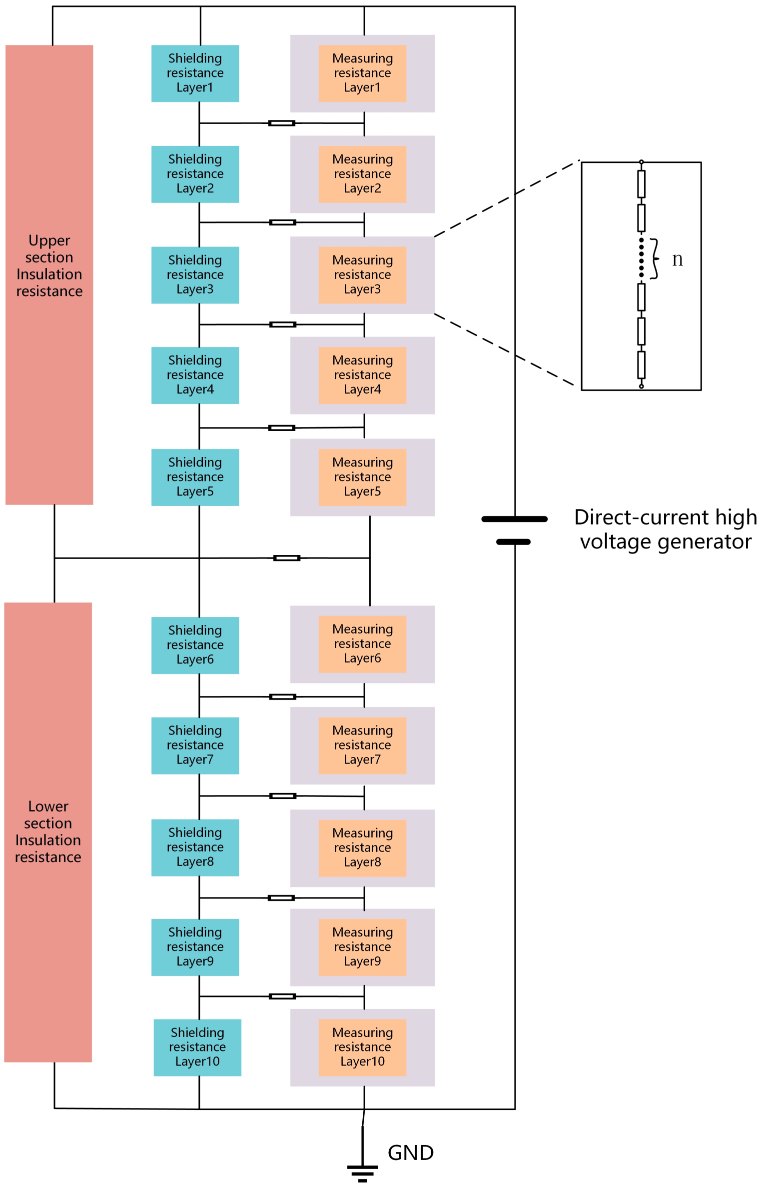

Figure 15. The resistance network model of the 2 × 550 kV DC voltage proportional standard device.

In this model, the same voltage is applied to the insulation resistance, the measurement resistance and the shielding resistance, which are equivalent to the insulation outer cylinder and grounded after the lower end of the measurement resistance is connected to the low-voltage resistance. The insulation resistance and the lower end of the shielding resistance are grounded. Then, the ratio of the applied voltage to the low-voltage end voltage is calculated, which is the voltage division ratio:

$$K = \frac{U}{u} = \frac{R_h I_h + R_l I_l}{R_l I_l} \tag{13}$$

Ignoring the leakage current between the brackets, then

$$K = 1 + \frac{R_h}{R_l} \tag{14}$$

5.2. The Calculation and Analysis of Voltage Division Ratio

We applied the NCIR neural network model into the equivalent resistance network model for calculation, and the calculation results are as follows (Figure 16).

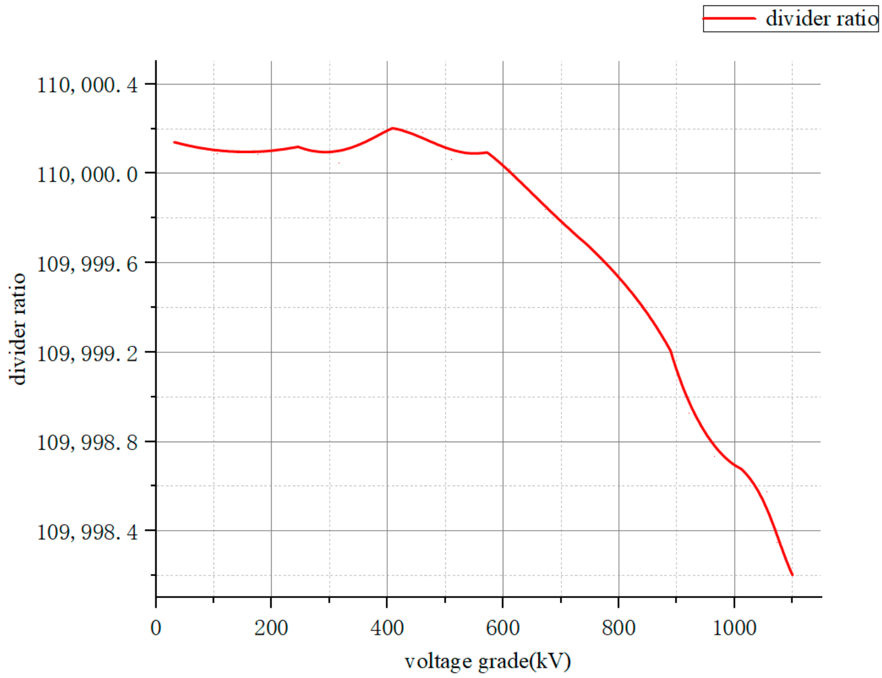

Figure 16. Calculation results of voltage divider ratio.

It can be seen form the figure that when the voltage level is low, the partial pressure is relatively stable, floating around 11,000. With the increase in the voltage grade, the insulation resistance changes greatly, resulting in the change in the voltage divider ratio. Under high field strength, the insulation resistance shows a decreasing trend. Therefore, the high-voltage end resistance, which is equivalent to the insulation resistance, measurement resistance, shielding resistance and insulation brackets in series and parallel also shows a decreasing trend, which ultimately results in a decrease in the voltage division ratio. At 1100 kV, the voltage divider ratio is 109,998.203 and the relative error is 1.634×10^{-5}.

In order to reduce the influence of the change in the voltage divider ratio on the 2×550 kV DC voltage proportional standard device to improve the measurement accuracy of the device, it can be improved from two aspects: optimizing the electric field distribution and reducing the influence of the insulation resistance on the measurement resistance midpoint potential.

Firstly, by optimizing the size and distribution of the electric field, the structure and position of the equalizing ring can be adjusted to improve the uniformity of the electric field and reduce the influence of the electric field gradient change on the voltage divider ratio. At the same time, this improved design can effectively reduce the interference of corona effect and other uncertain factors on the measurement results.

Secondly, in order to further improve the accuracy, a layer of shielding resistance can also be added to the device. There is only one shielding resistance layer between the insulation resistance and the measurement resistance in the traditional DC voltage proportional standard device, which can easily lead to the insulation resistance directly influencing the midpoint potential of the measurement resistance through the shielding resistance, and then causing deviation to the measurement results. By increasing the second layer of shielding resistance, a two-layer shielding structure is established between the insulation resistance and the measurement resistance, which can effectively reduce the interference caused by the direct connection between the insulation resistance and the shielding resistance, effectively improving the accuracy and stability of the measurement system. However, considering the factors such as material cost, manufacturing cost and resistance calorific value, building three or more layers of shielding resistance cannot achieve an optimization effect, so using two layers of shielding resistance is the better choice.

In this paper, the data are calculated and compared after a layer of shielding resistance is added. The results of the voltage divider ratio of the standard device are as follows (Figure 17).

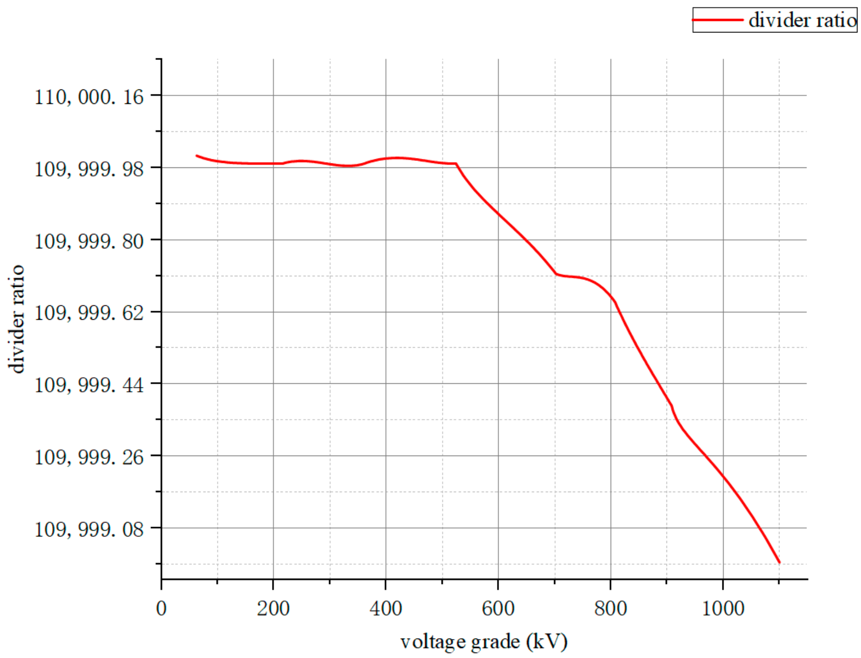

Figure 17. The voltage divider ratio calculation result after adding a layer of shielding resistance.

It can be seen that the voltage divider ratio is still relatively stable under the low-voltage grade. When the voltage is above 500 kV, the voltage divider ratio shows a downward trend, but it is relatively gentle compared with the trend before optimization, and the voltage divider ratio changes is relatively little. At 1100 kV, the voltage divider ratio is 109,998.994, and the relative error is 9.15×10^{-6}. Compared with one layer of shielding resistance, the error of the voltage divider ratio is reduced by 44%, which improves the influence of nonlinear change in insulation resistance on the accuracy of standard device.

6. Discussion

The results of this study reveal that the nonlinear characteristics of insulation resistance have a significant impact on the voltage dividing ratio in high-voltage DC systems. Consistent with previous studies, the results support the understanding that increases in voltage and electric field strength exacerbate the nonlinear behavior of insulating materials, leading to a decrease in resistance and thus affecting voltage measurement accuracy. This paper designs a new NCIR neural network to accurately fit nonlinear insulation data under various environmental conditions, and it obtains an accurate mapping between insulation resistance and influencing factors such as electric field strength, temperature and humidity. The implementation of a double-layer shielding resistor structure significantly reduces measurement errors compared to traditional single-layer shielding. This double-layer approach reduces the interference of nonlinear resistance effects and improves the accuracy and reliability of voltage division. The results show that under high-voltage conditions, the voltage divider ratio accuracy is improved by 44%.

The significance of these findings underscores the importance of optimized insulation design in China's expanding UHV transmission system, which is critical to supporting stable large-scale power transmission. Future research could explore alternative insulating materials that reduce nonlinearity under extreme conditions and further refine the network model to accommodate higher voltage ranges. In addition, integrating real-time environmental feedback into the voltage measurement model may help improve system responsiveness and adaptability to environmental fluctuations.

7. Conclusions

In this paper, a nonlinear resistance measurement platform for insulating materials is built. The resistance values of insulation resistance under different electric field strength, temperature and humidity are measured. The NCIR neural network is also designed to calculate the measured data. A resistance network model of a DC voltage proportional standard device is established, and the variation in division ratio under different voltages is calculated. The following conclusions are obtained.

In order to analyze the nonlinear conduction characteristics of insulating materials under high voltage, a measurement platform is designed and built in this paper. This platform can accurately measure the surface resistance and body resistance of insulating materials under different electric field strength, temperature and humidity conditions.

In order to effectively analyze the influence of electric field intensity, temperature and humidity on the nonlinear variation in insulation resistance, the NCIR neural network model is constructed. In this paper, the neural network models of different layers are compared, and the effect is the best when the number of fully connected layers is three. The MAE, MSE and RMSE of the model are all the smallest. The NCIR neural network can accurately fit the nonlinear characteristics of the insulation materials.

In this paper, the resistance network model of the DC voltage proportional standard device is established. By analyzing the series-parallel effect of insulation resistance, measurement resistance and shielding resistance and calculating the variation in voltage division ratio under different voltages, a method of adding one layer of shielding resistance is proposed. Compared with the single-layer shielding resistance layer, the DC voltage of the double-layer shielding resistance layer is reduced from 109,998.203 to 109,998.994, and the relative error is reduced from 1.634×10^{-5} to 9.15×10^{-6} with a relative error reduction of 44%.

Author Contributions: Conceptualization, Y.G. and X.C.; methodology, Y.G. and Y.D.; software, M.H. and R.G.; validation, W.Z., C.W. and M.H.; formal analysis, L.Q.; investigation, W.Z. and Z.C.; resources, F.L. and Z.C.; data curation, L.Q.; writing—original draft preparation, Y.G.; writing—review and editing, L.Z. and Y.G.; visualization, Y.G.; supervision, W.Z. and Z.C.; project administration, R.G. and Y.D.; funding acquisition, W.Z. All authors have read and agreed to the published version of the manuscript.

Funding: This research was funded by the State Grid Corporation of China Headquarters Science and Technology Project: Key Technology Research on Self-calibration and On-site Transfer of 1100 kV DC Voltage Ratio Magnitude, grant number No. 5700-202320616A-3-2-ZN.

Data Availability Statement: Restrictions apply to the datasets. The datasets presented in this article are not readily available because the data are part of an ongoing study; further inquiries can be directed to the corresponding author.

Acknowledgments: This paper benefited from the efforts and guidance of mentor Qin Liang, He Min, and the dedication and efforts of Ximing Chen, Duan Yuqing, Ran Gao, Chao Wang, Zheng Chen, Fei Lin and Lei Zhuang State Grid Anhui Electric Power Company Limited.

Conflicts of Interest: Authors Yin Gao, Ximing Chen, Yuqing Duan, Ran Gao, Chao Wang, Zheng Chen, Fei Lin and Lei Zhuang were employed by the company State Grid Anhui Electric Power Company Limited. The remaining authors declare that the research was conducted in the absence of any commercial or financial relationships that could be construed as a potential conflict of interest.

References

1. Liu, Z. *Ultra-High Voltage Alternating Current and Direct Current Grids*; M. China Electric Power Press: Beijing, China, 2013.
2. Wang, C.; Song, Y. Regional distribution and transmission status of supply and demand of electricity resources in China. *J. Chin. Grid Clean Energy* **2015**, *31*, 69–74.
3. Shu, Y.; Zhang, W. Research on several key technologies of ultra-high voltage transmission. *J. Chin. China J. Electr. Eng.* **2007**, *27*, 1–6.
4. Huang, D.; Shu, Y.; Ruan, J.; Hu, Y. Ultra-high voltage transmission in China: Developments, current status and future prospects. *J. Proc. CSEE* **2009**, *97*, 555–583.
5. Liang, X.; Zhang, P.; Chang, Y. Status quo and development prospect of high-voltage direct current transmission technology. *J. Chin. Power Grid Technol.* **2012**, *36*, 1–9.
6. Li, D.; Liu, G.; Li, Q.; Li, H.; Hu, H.; Xiong, Q.; Yang, C. Measurement of temperature coefficient and voltage coefficient of precision resistors under high voltage. *J. Chin. Electr. Meas. Instrum.* **2012**, *49*, 20–24.
7. Zhang, R.; Chen, C.; Wang, C. *High Voltage Testing Technology*; M. Tsinghua University Press: Beijing, China, 2002.
8. Zhang, H.; Lin, F.; Shao, H.; Zhang, Z. Study on leakage current measurement of DC high-voltage resistive voltage divider. *J. Chin. J. Metrol.* **2018**, *39*, 83–88.
9. Meng, X.; Mei, H.; Chen, C.; Wang, L.; Guan, Z.; Zhou, J. Mechanistic study on the development characteristics of insulating dielectric surface flow injection. *J. Chin. Chin. J. Electr. Eng.* **2013**, *33*, 155–165.
10. Zhang, S.; Zhou, Y.; Li, D.; Wang, T.; Li, Q.; Li, H. Field calibration test of DC voltage transformer in ±800 kV converter station. *J. Chin. High Volt. Technol.* **2011**, *37*, 2119–2125.
11. Sharifi, E.; Cherney, E.A.; Jayaram, S.H. Anisotropic dielectric properties of stress grading materials used in medium voltage form-wound motor coils to study thermal effects of repetitive fast pulses. In Proceedings of the 2009 IEEE Electrical Insulation Conference, Montreal, QC, Canada, 31 May–3 June 2009; pp. 333–337.
12. Schmerling, R.; Jenau, F.; Staubach, C.; Pohlmann, F. Investigations of modified nonlinear electrical materials for end corona protection in large rotating machines. In Proceedings of the 2012 47th International Universities Power Engineering Conference (UPEC), Uxbridge, UK, 4–7 September 2012; pp. 1–5.
13. Alireza, P.L.; Ko, Y.T.C.; Gillett, J.; Petrone, C.M. Superconductivity up to 29 K in $SrFe_2As_2$ and $BaFe_2As_2$ at high pressures. *J. Phys. Condens. Matter* **2009**, *21*, 012208. [CrossRef]
14. Li, Y.; Yao, X.; Sun, J.; Tian, X.; Chen, J. Moisture-heat aging characteristics of epoxy resin curing compounds for insulation encapsulation. *J. Chin. High Volt. Technol.* **2021**, *47*, 3600–3607.
15. Zhang, Y.; Liu, P.; Liu, X.; Hu, B.; Liang, Z. Effect of temperature on the nonlinear resistance characteristics of corona-proof materials for high-voltage motors. *J. Chin. Insul. Mater.* **2021**, *54*, 86–91.
16. Elg, A.P.; Bergman, A.; Hällström, J.; Kharezy, M.; Nieminen, T. Traceability and Characterization of a 1000 kV HVDC Reference Divider. *IEEE Trans. Instrum. Meas.* **2015**, *64*, 1709–1715. [CrossRef]
17. Wang, C.; Zhang, L.; Zhang, G. Research on the nonlinear mechanism of DC resistance voltage divider. *Acta Metrol. Sin.* **2022**, *43*, 521–525.
18. Barros, R.L.G.; Kelleners, M.H.; van Bemmel, L.; van der Leegte, T.V.; van der Schaaf, J.; de Groot, M.T. Elucidating the increased ohmic resistances in zero-gap alkaline water electrolysis. *J. Electrochim. Acta* **2024**, *507*, 145161. [CrossRef]

19. Sun, K.; Li, X.; Mei, Y. Research on design elements of nonlinear conductive composites doped with silicon carbide particles for insulating encapsulation. *J. Mech. Eng.* **2024**, 1–9. Available online: http://kns.cnki.net/kcms/detail/11.2187.TH.20241010.1127.008.html (accessed on 7 November 2024).
20. Nanung, Y.; Tangjang, L.; Das, H.; Kalita, P.K. Poole-Frenkel conduction in CdS single-layered and CdS/SnS_2 heterojunction electrode system. *J. Nano-Struct. Nano-Objects* **2024**, *40*, 101359. [CrossRef]
21. Asgari, A.; Bagheri, M.; Hadizadeh, M. Advanced seismic analysis of soil-foundation-structure interaction for shallow and pile foundation in saturated and dry deposits: Insights from 3D parallel finite element modeling. *J. Struct.* **2024**, *69*, 107503. [CrossRef]
22. Ma, R.; Liu, G.; Liu, N.; Liu, X.; Wang, J. Finite element analysis of improved structure of current transformer rain cover based on ANSYS. *Mech. Eng. Autom.* **2023**, *4*, 63–64, 67.